Biogeotechnics 4 (2026) 100186

Contents lists available at ScienceDirect

Biogeotechnics

journal homepage: www.keaipublishing.com/en/journals/biogeotechnics/

Pore-scale investigation of shielding effects on $CaCO_3$ dissolution rate in limestone-based microfluidics

Yanan Zhang[a,b], Ran Hu[a,b,*], Chenxing Zhou[a,b,*], Zhi-Bing Yang[a,b], Yifeng Chen[a,b]

[a] State Key Laboratory of Water Resources and Hydropower Engineering Science, Wuhan University, Wuhan 430072, China
[b] Key Laboratory of Rock Mechanics in Hydraulic Structural Engineering of the Ministry of Education, Wuhan University, Wuhan 430072, China

ARTICLE INFO

Keywords:
Limestone-based microfluidic
Coupled dissolution and precipitation
$CaCO_3$ dissolution
Shielding effects
Secondary precipitation

ABSTRACT

The coupled mineral dissolution-precipitation process plays a critical role in natural and engineered systems with fluid-rock interaction including geological CO_2 sequestration and contamination treatment of groundwater. A representative scenario is the reaction between limestone and acidic, sulfate-bearing solutions, where the dissolution of carbonate minerals drives gypsum precipitation. Previous studies have investigated the impact of this coupled process on hydraulic parameters through core-flooding experiments. However, the interplay between calcite dissolution ($CaCO_3$) and secondary precipitation ($CaSO_4$) as well as its influence on the reaction rate of $CaCO_3$ remains unclear. Here, we combine flow visualization experiments in limestone-based microfluidics with post-experiment SEM-EDS characterization to probe how sulfate concentration affects both precipitation morphology and $CaCO_3$ dissolution rates under the same pH condition (pH = 1). Two distinct dissolution-precipitation coupling regimes have been identified. At low sulfate concentrations, the dissolution-dominated regime causes continuous dissolution of limestone throughout experiments because the porous gypsum layer permits continuous acid infiltration into the rock surfaces. Conversely, high sulfate concentrations induce a precipitation-dominated regime, reducing dissolution rates by an order of magnitude as a dense, thick layer completely shields the reactive surface area. We find a critical sulfate concentration threshold that triggers regime transition, wherein the released calcium concentration equilibrates with the supplied sulfate in solution, facilitating the formation of a dense coating layer. Quantified results indicate that the average dissolution rate decreases linearly with the saturation index by one order of magnitude as sulfate concentration increases from 0 to 0.2 mol/L. These findings provide insights into coupled geochemical processes and offer practical guidance for predicting reaction rates in reactive transport modeling.

1. Introduction

The coupled mineral dissolution-precipitation process is important in many engineering such as carbon capture and storage (CCS) (Sabo & Beckingham, 2021; Wang et al., 2023), environmental remediation of polluted water (Kampman et al., 2014; Klasa et al., 2013; Prieto et al., 2013) and oil reservoir exploitation (Crowe, 1986; Rege & Fogler, 1989). When CO_2 is injected into a salinity aquifer, water saturated with CO_2 dissolves the host rock, and then carbonate reacts with the released cations to form secondary carbonate mineral deposits (Daval et al., 2009; Ma et al., 2023; Oelkers & Schott, 2005). The coupled dissolution-precipitation process may form a layer over the surface of primary minerals and have a significant impact on the subsequent reaction rates and the sequestration efficiency of carbon mineralization (Stockmann et al., 2011, 2013; Tian et al., 2015; Yang et al., 2020). However, how the coupled mineral dissolution and precipitation process affects flow pathways and mass transfer within the geological system remains poorly understood.

Numerous studies have elucidated the evolution of hydraulic parameters in fractured porous media under either dissolution or precipitation processes (Akindipe et al., 2021; Chen et al., 2024). For coupled dissolution-precipitation systems, previous works have revealed that the pore structure alteration and hydraulic parameters evolution are influenced by flow velocity, solute concentration, and fracture geometry (Jayasekara et al., 2020; Jiang et al., 2025; Poonoosamy et al., 2020). Using acidic, sulfate-bearing solutions infiltrating the limestone core, previous experiments examined the competition between calcite dissolution and gypsum precipitation and their impacts on permeability evolution (De Graaff et al., 1997; Singurindy & Berkowitz, 2003, 2005). While these works have developed conceptual

* Corresponding authors.
E-mail addresses: whuran@whu.edu.cn (R. Hu), cxzhou@whu.edu.cn (C. Zhou).

https://doi.org/10.1016/j.bgtech.2025.100186
Received 13 April 2025; Received in revised form 16 May 2025; Accepted 8 June 2025
Available online 8 June 2025
2949-9291/© 2026 The Authors. Publishing services by Elsevier B.V. on behalf of KeAi Communications Co. Ltd. This is an open access article under the CC BY license (http://creativecommons.org/licenses/by/4.0/).

models describing dissolution-precipitation coupling regimes across different concentration and flow rate conditions, they still lack dynamic observations and quantitative characterization of the coupled mineral dissolution-precipitation processes, and the interplay between dissolution and precipitation remains unclear. To bridge this knowledge gap, we performed visualization experiments to probe the interplay between flow, dissolution, and precipitation processes in limestone-based microfluidics at different sulfate ion concentrations.

2. Materials and methods

In this study, limestone samples are employed for the flow-through microfluidic experiments (Supporting Information Fig. S1), including calcite ($CaCO_3$) dissolution and gypsum ($CaSO_4$) precipitation. The XRD analysis demonstrates that the mass fraction of calcite and dolomite is about 75% and 25%, respectively. The fabrication of the microfluidics is shown in Fig. 1. Firstly, limestone is polished to a thickness of 200 μm and cut into square pieces with sides of 7 mm (Fig. 1A). Then, the samples are divided into two pieces and placed in a Polydimethylsiloxane (PDMS) cell. During the placement of the rock slices, the average fracture aperture was controlled at 200 μm, with the aperture of the inlet (~200 μm) serving as the reference (Supporting Information Fig. S2). Finally, a glass slide is coated with a thin PDMS layer and then bonded with the PDMS flow cell to fabricate a rock-based microfluidic device. The microfluidic chip is quasi-two-dimensional (quasi-2D), which enables direct observation of heterogeneous mineral surface evolution (Ling et al., 2022; Zhou et al., 2023). To study the reaction process and under the combined influence of flow, dissolution, and precipitation, a fluorescence microscope coupled with a high-speed CMOS camera is employed to capture the bubble generation and the rock surface evolution at the channel scale (Fig. 1B). After the experiment, the limestone pieces are taken out from the microfluidic chip and placed at the sample stage to dry at 75 °C for 24 h. The high-resolution Scanning Electron Microscope (SEM) imaging and energy-dispersive spectroscopy (EDS) are used to characterize the microstructure of the precipitate layer at the pore scale (Fig. 1C).

Before the experiment, we saturate the microfluidics with deionized (DI) water. Then, acid solutions with different hydrogen/sulfate ion concentrations ($C(H^+/SO_4^{2-})$) are injected into the microfluidic model at a constant flow rate of $Q = 24$ μL/min. After the reactive fluid is injected, Ca^{2+} is released from the rock surfaces due to calcite dissolution. Then, the released Ca^{2+} bonds with SO_4^{2-} in the solution at the solid-fluid interfaces, nucleates on the rock surface, and grows into a precipitate layer with different structures. The chemical reactions for calcite dissolution and gypsum precipitation are as follows:

$$CaCO_3 + 2H^+ \rightarrow Ca^{2+} + CO_2 + H_2O \quad (1a)$$

$$Ca^{2+} + SO_4^{2-} + 2H_2O \rightarrow CaSO_4 \cdot 2H_2O \quad (1b)$$

To study the impact of fluid concentration on the coupled dissolution-precipitation process, we conducted a total of 10 experiments with mixed

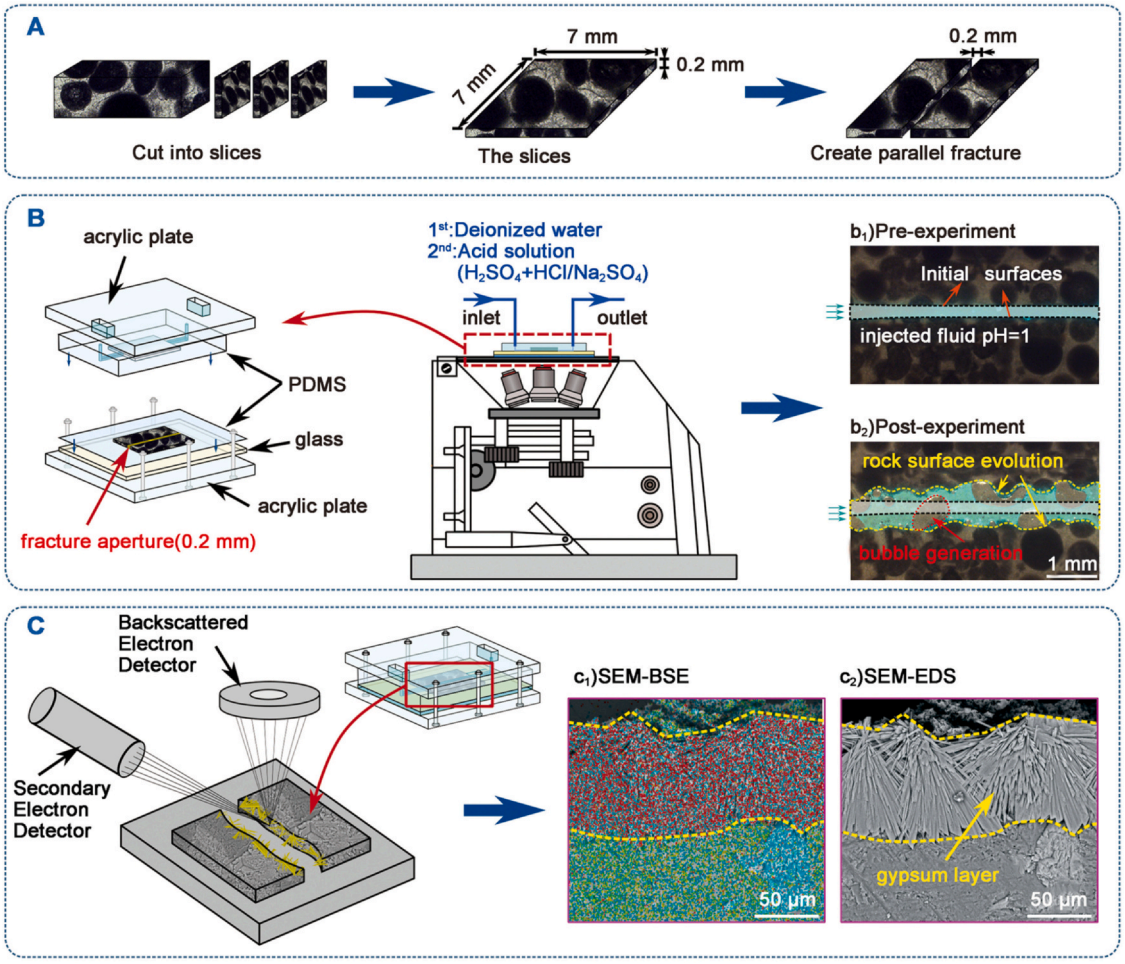


Fig. 1. Experimental procedure: (**A**) Fabrication of the limestone samples. The limestone is cut into ~7 × 7 mm^2 slices and polished into ~0.2 mm pieces. Then, the slices are divided into two pieces to create a fracture channel. (**B**) Microfluidic experiments. The sample pieces are placed into the PDMS flow cell and the initial aperture between the two rock pieces is controlled as 0.2 mm. The flow cell is bonded with a glass slide coated with a thin layer of PDMS. Then, the flow-through experiments are conducted in the microfluidics and the reaction process is captured by a fluorescence microscope. (**C**) Post-experiment characterization. The post-experiment samples are taken out of microfluidic models and mounted on the conductive stage for high-resolution characterization via SEM-BSE and EDS.

Table 1
Composition of the injected solution for all experiments.

Exp. #	Mixtures	$C(H^+)$ /(mol/L)	$C(SO_4^{2-})$ /(mol/L)
1	2 mL HCl + 18 mL H_2O	0.1	0
2*			
3	1 mL HCl + 1 mL H_2SO_4 + 18 mL H_2O		0.025
4*			
5	2 mL H_2SO_4 + 18 mL H_2O		0.05
6*			
7	2 mL H_2SO_4 + 2 mL Na_2SO_4 + 16 mL H_2O		0.1
8*			
9	2 mL H_2SO_4 + 6 mL Na_2SO_4 + 12 mL H_2O		0.2
10*			

* The asterisk represents the repeated experiment. The initial concentrations of HCl, H_2SO_4, and Na_2SO_4 are 1 mol/L, 0.5 mol/L, and 0.5 mol/L, respectively.

acid solutions (with the same pH of 1) at five different concentrations, as shown in Table 1. Each experiment is repeated once. Reactive solutions are produced using hydrochloric acid (HCl), sulfuric acid (H_2SO_4), and sodium sulfate (Na_2SO_4), with concentrations of 1 mol/L, 0.5 mol/L, and 0.5 mol/L, respectively. H_2SO_4 and Na_2SO_4 are used to adjust the sulfate ion concentration in the solution, and HCl is used to adjust the initial pH. The injected solutions were prepared by mixing these solutions with deionized water to achieve the target sulfate concentrations and constant pH, as shown in Table 1. The mixtures were then stirred for 5 min to ensure homogeneity and degassed in a vacuum chamber for 20 min.

The pH of injected solutions is 1 and the *Pe* number equals 1000 for all experimental conditions. Here, *Pe* is defined as $Pe = v < b_0 > /D_m = Q/(WD_m)$ (Dijk & Berkowitz, 1998; Szymczak & Ladd, 2009), where v is the flow rate defined as $v = Q/(< b_0 > W)$; Q is the volume flow rate with $Q = 24\,\mu L/min$; $< b_0 >$ is the fracture aperture with $< b_0 > = 0.2$ mm; W is the thickness of the fracture channel with $W = 0.2$ mm; D_m is the molecular diffusion coefficient with $D_m = 2 \times 10^{-9}$ m^2/s.

3. Results

The dynamic dissolution-precipitation process images are shown in Fig. 2A. As the reactive fluid is continuously injected, the limestone is gradually dissolved, leading to generation of CO_2 bubbles and

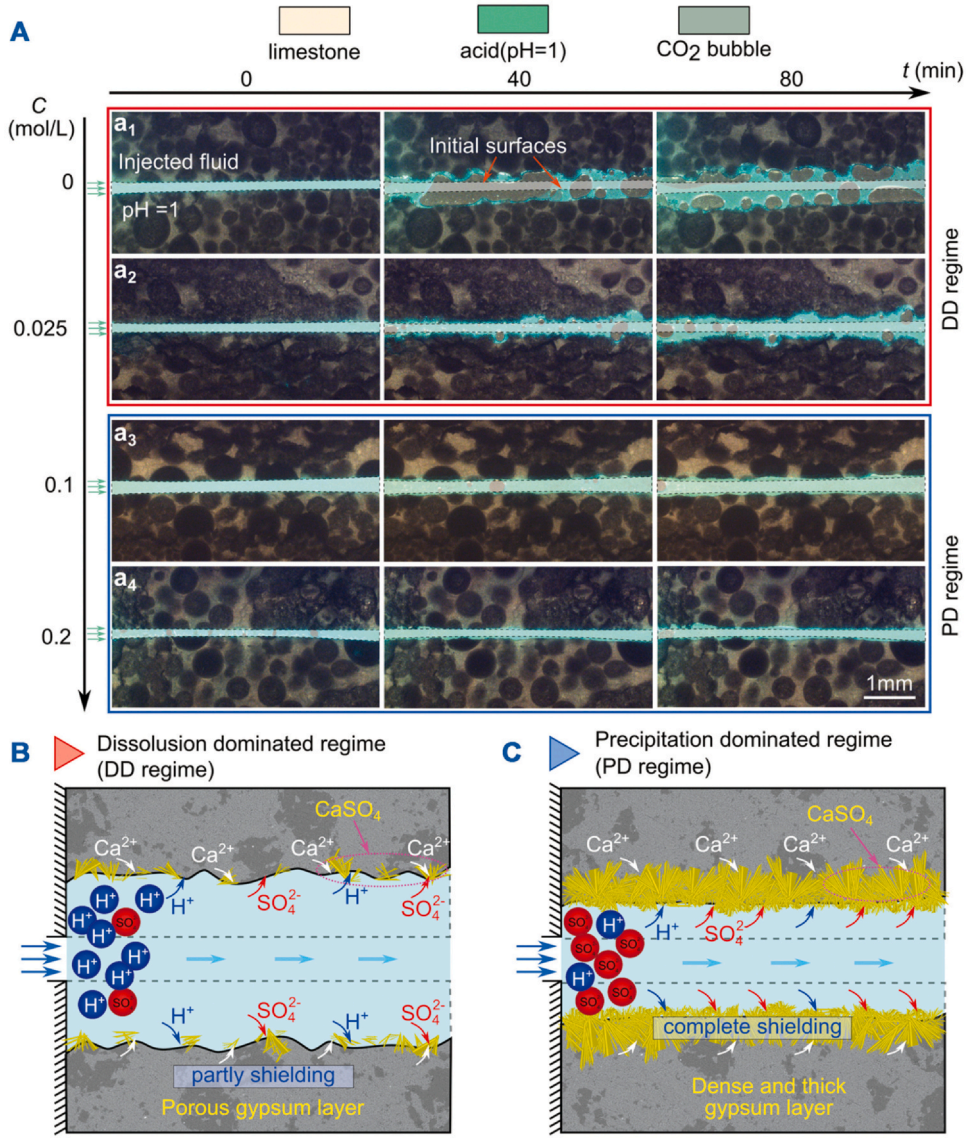


Fig. 2. The dynamic images of the coupled dissolution-precipitation process in the fracture channel at varying sulfate concentrations (pH = 1). (**A**) The temporal evolution of dissolution morphology at four different sulfate concentration conditions. The sulfate concentration increases from the top to the bottom, with the initial solid-fluid interfaces indicated by the black dashed lines. The acid (liquid) and CO_2 (gas) are represented in green and light brown, respectively. Two distinct coupled dissolution-precipitation regimes are observed, denoted as the DD regime and the PD regime. In the DD regime (**B**), the mineral reaction is dominated by dissolution. In contrast, in the PD regime (**C**), the process is dominated by precipitation.

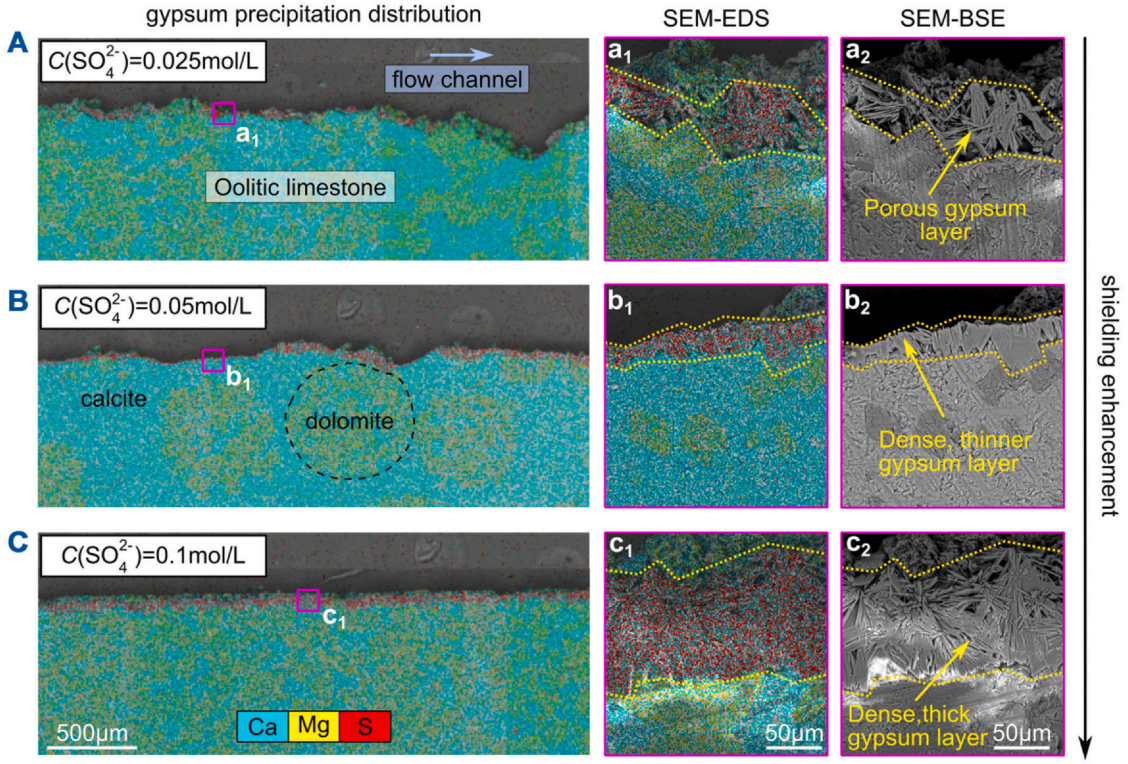


Fig. 3. The SEM-BSE and EDS images of the post-experiment samples: (**A**) The porous gypsum precipitate layer on the rock surface at low sulfate concentrations; (**B**) The dense and thin gypsum layer on the surface at moderate sulfate concentrations; (**C**) The dense and thick gypsum layer on the rock at high sulfate concentrations.

enlargement of fracture aperture (from left to right in Fig. 2A). As the sulfate concentration increases, the total dissolved volume tends to decrease (from top to bottom in Fig. 2A), as supported by Supporting Information Fig. S4. From the experimental phase diagram, we observe a competition between dissolution and precipitation, leading to two distinct coupled dissolution-precipitation regimes (Fig. 2B and 2C). At low sulfate concentration conditions ($C(SO_4^{2-}) < 0.05$ mol/L), the final dissolved volume of limestone is relatively large (Fig. 2a_1 and a_2). The rate of CO_2 bubble generation is relatively high throughout the entire reaction process (Supporting Information Movie S1), indicating that the dissolution reaction is continuously occurring at a relatively high rate. In this regime, the reaction process is dissolution-dominated (abbreviated as the DD regime). This phenomenon suggests that the gypsum precipitate layer is a porous structure which can allow the acid to infiltrate through and continuously dissolve the rock (Fig. 2B). At higher sulfate concentration conditions ($C(SO_4^{2-}) > 0.05$ mol/L), although the rate of CO_2 bubble generation is high at the initial moment, it significantly decreases within a short period (Supporting Information Movie S2). It suggests that the dissolution-precipitation process is precipitation-dominated (abbreviated as the PD regime).

The pore-scale mechanism of the coupled dissolution-precipitation regimes is confirmed by post-experiment SEM and EDS analysis (Fig. 3). It shows that a new needle-shaped mineral is observed on the surfaces of the fracture channels, which has significant differences from the microstructure of the limestone. The needle-shaped mineral on the solid-liquid interfaces is identified as gypsum based on the EDS analysis. When the rock-fluid interfaces are present, the heterogeneous nucleation of gypsum at the interfaces is more favorable compared with homogeneous nucleation within the bulk solution because the nucleation energy barrier at the interfaces is lower than that in the solution (Li & Deepak, 2022; Sudmalis & Sheikholeslami, 2000). This leads to the precipitation of calcium sulfate on the rock surface, which subsequently develops into a precipitate layer. In the EDS images, calcite, dolomite, and gypsum precipitations are denoted by blue, yellow, and red, respectively. Calcium carbonate dissolution is a transport-limited process, mainly controlled by the diffusion of reactants/products at the solid-fluid interfaces (Singurindy & Berkowitz, 2005). At low sulfate concentration conditions (Fig. 3A), gypsum precipitations form sparsely at mineral-fluid interfaces, creating a porous gypsum layer (Fig.3a_2). This permeable structure allows continuous H^+ diffusion to the carbonate surface, enabling sustained dissolution throughout the experiment. In contrast, high sulfate concentration conditions promote uniform precipitation across the fracture surface that effectively isolates the limestone from acid solutions and terminates dissolution (Fig. 3C). At moderate sulfate concentration ($C(SO_4^{2-}) = 0.05$ mol/L) although the density of the precipitation exceeds that of low-concentration conditions (Fig.3b_1), the layer remains insufficiently thick to fully inhibit calcite dissolution. Moreover, precipitation occurs heterogeneously along the fracture channel, leaving significant reactive surface areas exposed to the acid solution (Fig. 3B). These results indicate that there is a transition from the dissolution-dominated regime to the precipitation-dominated regime.

According to chemical reaction (Eq. (1b)), gypsum precipitation kinetics are governed by both Ca^{2+} concentration derived from calcite dissolution and sulfate concentration supplied by the injected solution. Under high flow rate conditions ($Q = 24$ μL/min, $Pe = 1000$) and constant pH conditions (pH = 1) in our experiments, the strong advection effect results in uniform dissolution throughout the fracture channel. At the initial stage of the reaction, we assume that hydrogen ions fully react with the rock at the solid-fluid interface, so the maximum Ca^{2+} concentration released from the limestone dissolution equals half the H^+ concentration (0.05 mol/L, chemical reaction 1a). When sulfate concentration reaches this equilibrium Ca^{2+} concentration (0.05 mol/L), the dissolved Ca^{2+} rapidly combines with SO_4^{2-}, generating dense precipitates on the rock surfaces. A basic stoichiometric approach based on the chemical reaction Eq. (1a) and Eq. (1b) can be represented as follows:

$$C_{cri} = C_{Ca^{2+}} = \frac{1}{2} C_{H^+} \tag{2}$$

where C_{cri} is the critical sulfate concentration, $C_{Ca^{2+}}$ is the maximum released calcium ion concentration, and C_{H^+} is the hydrogen ion concentration of the injected acid solution. This equation indicates that a critical

concentration triggering regime transition is $C(SO_4^{2-}) = 0.05$ mol/L, corresponding to a critical H^+/SO_4^{2-} concentration ratio of 2:1 (Fig. 3B). This critical concentration may also be affected by the pH value. When the pH value is lower, the dissolution reaction can provide enough Ca^{2+} for gypsum crystallization, and the critical concentration is determined by Eq. 2. However, the Ca^{2+} concentration generated by the higher pH may be insufficient, causing the solution to remain unsaturated and thereby inhibiting the crystallization of gypsum.

To further quantify how the precipitation coating layer affects the dissolution rates, we calculate the temporal average dissolution rate (R_t) for the two regimes. The dissolution rates are obtained through image segmentation and post-processing since the limestone piece is a quasi-two-dimensional (quasi-2D) chip (~ 200 μm). The details of image-postprocessing can be seen in Supporting Information Fig. S3.

$$R_t = \frac{\Delta V_{(t)}}{\Delta t} \tag{3}$$

where $\Delta V_{(t)}$ is the fracture dissolved volume over the time interval Δt.

To compare the evolution of R_t under different conditions, we define the relative dissolution rate (r) as:

$$r = \frac{R_t}{R_0} \tag{4}$$

where R_t is the temporal average dissolution rate and R_0 is the initial dissolution rate.

Fig. 4A shows the temporal evolution of R_t at different sulfate concentrations. The dimensionless time is defined as the time normalized by the total dissolution time (T_f). For all experiments, the dissolution rate of $CaCO_3$ gradually decreases over time and eventually stabilizes, despite the injected solution being pure HCl. This phenomenon may be caused by the enlargement of the fracture aperture and the decrease in mass transfer rate across the aperture (Zhou et al., 2022). The formation of gas bubbles may also be another reason for the reduction of the dissolution rates. De Graaff et al. (1997) attribute this to the gradual decrease in H^+ concentration as the reaction proceeds. Although the gypsum layer reduces the effective reaction area and the contact between acid and carbonate for all experiments, the relative dissolution rates at the final time for different regimes are distinct. In the DD regime, r decreases slowly and stabilizes at about 0.2, indicating that the dissolution still occurs at the final time. In the PD regime, r decreases rapidly until it approaches 0, indicating that the dissolution nearly terminates at the final time. This quantitative result demonstrates that the evolution of macroscopic dissolution rates is controlled by the microscopic structure of the precipitations, as illustrated in Fig. 3.

4. Discussion

The composition of the injected solution induced distinct precipitation patterns, thereby influencing the subsequent dissolution of the limestone. The precipitation of calcium sulfate depends on the supersaturation (Sudmalis & Sheikholeslami, 2000), and the saturation index (SI) is used to characterize the supersaturation of $CaSO_4$ in the system. SI is calculated by PHREEQC software (Supporting Information Table S1), which is defined as $SI = \log(IAP) - \log(K_{sp})$, where IAP is the ion activity product of gypsum and K_{sp} is the thermodynamic solubility product constant of gypsum. To further explore how gypsum precipitation affects the dissolution rates of $CaCO_3$, we analyze the relationship between the saturation index (SI) and the average dissolution rate R_{avg} (Fig. 4B). Since the volume of gypsum precipitation is negligible, the average dissolution rate (R_{avg}) during the reaction process can be defined as:

$$R_{avg} = \frac{V_f}{T_f} \tag{5}$$

where V_f is the total dissolution volume and T_f is the total dissolution time.

It can be observed that as the SI increases, the average reaction rate significantly decreases. For $SI = 0.47$, the average dissolution rate is 1.63×10^{-5} mm^3/s, which has decreased by nearly one order of magnitude compared to the average dissolution rate under the condition of $C(SO_4^{2-}) = 0$ (Supporting Information Table S2). This indicates that the gypsum precipitate layer has a significant shielding effect on $CaCO_3$ dissolution rates. In the case of $SI = -0.17$ ($C(SO_4^{2-}) = 0.025$ mol/L), a small number of gypsum precipitations still form on the surface of calcium carbonate. This phenomenon may be attributed to the situation that the fluid may be supersaturated at the local solid-liquid interfaces even though the precipitation phase is an undersaturated solution in the bulk composition (Ruiz-Agudo et al., 2014). Results also indicate that the bulk parameter may be insufficient to characterize the local coupled dissolution-precipitation behavior. Furthermore, we find that the relationship between the R_{avg} and SI can be fitted well with the linear relationship, which can be written as:

$$\log R_{avg} = -1.1SI - 4.23 \tag{6}$$

where R_{avg} is the average dissolution rate of the entire reaction process and SI is the saturation index of gypsum at the initial time (Supporting Information Table S1). This relationship may guide the prediction of reaction rates for reactive transport modeling.

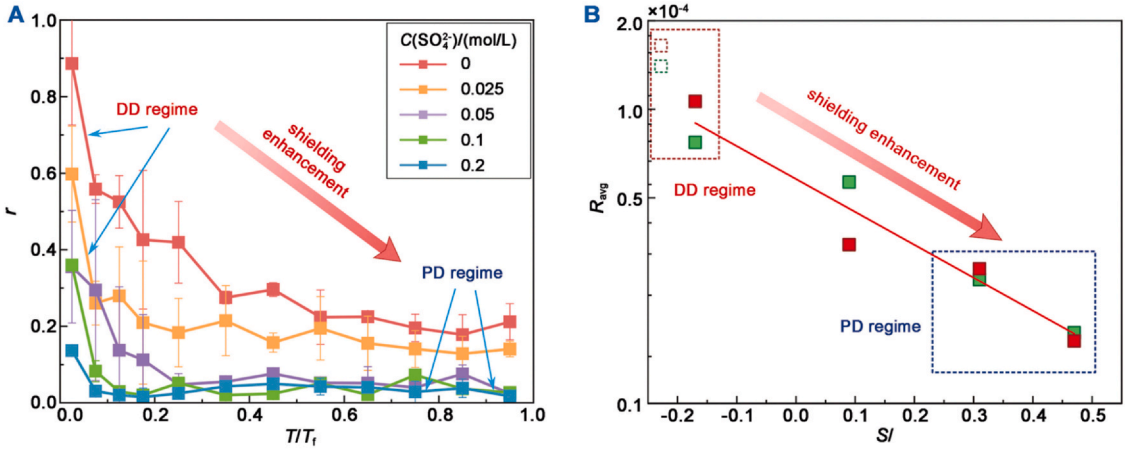


Fig. 4. (**A**) The variation of the relative dissolution rates (r) with normalized dimensionless time (T/T_f) at different sulfate concentrations. The stable value of r is 0.2 in the DD regime, while the stable value is lower than 0.1 in the PD regime; (**B**) The relationship between the average dissolution rate (R_{avg}) and the saturation index (SI). The red and green boxes represent two sets of duplicate experiments under the same conditions. The dashed box on the left represents the cases of pure HCl. As the SI increases, the average reaction rate shows a decreasing trend. The linear fit between Log(R_{avg}) and SI has a good correlation ($R^2 = 0.94$). Compared to the cases of pure HCl, R_{avg} decreases by nearly an order of magnitude at $SI = 0.47$.

Our experiments were conducted under constant flow rate conditions (Pe = 1000) and constant pH conditions (pH = 1). Fluid properties (e.g., pH, flow rate) and rock characteristics (e.g., surface roughness, mineral composition) may also influence the calcite dissolution, the nucleation sites, or nucleation rates of crystals (Alarji et al., 2022; Grosfils & Lutsko, 2021; Levenson et al., 2017; Xu & Liu, 2025), thereby affecting the subsequent dissolution-precipitation process. Although Eq. 6 is derived under the conditions of constant flow rate and pH, we can quantify the relationship between the R_{avg} and SI under varying fluid properties and rock samples using real-rock microfluidic experiments. To further investigate the influence of these factors on the interplay between dissolution and precipitation, the high spatiotemporal-resolution observation techniques, such as micro-PIV or confocal microscopy, will be required to investigate the dynamic evolution of gypsum. These technologies can reveal the formation mechanisms of porous and dense precipitate layers at the pore scale and provide insights for the coupled dissolution-precipitation process.

5. Conclusion

This study investigates the coupled calcite ($CaCO_3$) dissolution and gypsum ($CaSO_4$) precipitation process and its effect on dissolution rates in limestone-based microfluidics combining dynamic imaging of the dissolution process and high-resolution characterization of the post-experiment samples. The gypsum precipitated at the solid-liquid interfaces forms a porous/dense gypsum precipitate layer on mineral-fluid interfaces at different sulfate concentrations, reducing the reactive surface area and inhibiting the $CaCO_3$ dissolution rates. Two dissolution-precipitation coupling regimes are identified by direct observation and quantitative characterization of the limestone dissolution rates. At low sulfate concentrations ($C(SO_4^{2-}) < 0.05$ mol/L), the porous gypsum layer formed on the solid-fluid interfaces cannot inhibit acid infiltration into the porous layer, and the reaction process is dissolution-dominated during the experiments (the DD regime). At high sulfate concentrations ($C(SO_4^{2-}) > 0.05$ mol/L), a dense and thick gypsum layer coating on the rock surfaces completely shields the contact between the limestone and acid, causing a rapid decline of dissolution rates, and the reaction process is precipitation-dominated during the experiments (the PD regime). While at moderate sulfate concentration ($C(SO_4^{2-}) = 0.05$ mol/L), the reactive process is controlled by the competition between dissolution and precipitation. To quantify the shielding effect on the dissolution rates, we analyze the relationship between the average dissolution rate and the saturation index (SI), indicating a decrease of the average reaction rate by nearly one order of magnitude as the SI increases. These findings provide insights into pore-scale coupled dissolution-precipitation mechanisms and offer constraints for predicting reaction rates in large-scale reactive transport modeling.

CRediT authorship contribution statement

Yanan Zhang: Writing – review & editing, Writing – original draft, Methodology, Investigation, Formal analysis, Data curation. **Ran Hu:** Writing – review & editing, Writing – original draft, Supervision, Resources, Project administration, Methodology, Investigation, Funding acquisition, Formal analysis, Conceptualization. **Chenxing Zhou:** Writing – review & editing, Writing – original draft, Resources, Methodology, Investigation, Formal analysis, Conceptualization. **Zhi-Bing Yang:** Project administration. **Yifeng Chen:** Project administration.

Declaration of Competing Interest

Ran Hu is the editorial board member for Biogeotechnics, he was not involved in the editorial review or the decision to publish this article. The other authors declare that they have no known competing financial interests or personal relationships that could have appeared to influence the work reported in this paper.

Acknowledgements

This work was supported by the National Natural Science Foundation of China (52409142, 52379107, U2340228).

Open research

Details of experiments and the images can be found in Supporting Information S1, Supporting Information Movie1 and Movie2.

Appendix A. Supporting information

Supplementary data associated with this article can be found in the online version at doi:10.1016/j.bgtech.2025.100186.

References

Akindipe, D., Saraji, S., & Piri, M. (2021). Salt precipitation during geological sequestration of supercritical CO_2 in saline aquifers: A pore-scale experimental investigation. *Advances in Water Resources, 155*. https://doi.org/10.1016/j.advwatres.2021.104011

Alarji, H., Alzahid, Y., & Regenauer-Lieb, K. (2022). Acid stimulation in carbonates: Microfluidics allows accurate measurement of acidic fluid reaction rates in carbonate rocks by quantifying the produced CO_2 gas. *Journal of Natural Gas Science and Engineering, 99*. https://doi.org/10.1016/j.jngse.2022.104444

Chen, X., Hu, R., Zhou, C., Xiao, Y., Yang, Z., & Chen, Y. (2024). Capillary-driven backflow during salt precipitation in a rough fracture. *Water Resources Research, 60*(3), https://doi.org/10.1029/2023WR035451

Crowe, C. (1986). Precipitation of hydrated silica from spent hydrofluoric-acid - how much of a problem is it. *Journal of Petroleum Technology, 38*(12), 1234–1240. https://doi.org/10.2118/13083-PA

Daval, D., Martinez, I., Corvisier, J., Findling, N., Goffé, B., & Guyot, F. (2009). Carbonation of ca-bearing silicates, the case of wollastonite: Experimental investigations and kinetic modeling. *Chemical Geology, 265*(1), 63–78. https://doi.org/10.1016/j.chemgeo.2009.01.022

De Graaff, J. W. M., Schuiling, R. D., Speck, J. H. R., & Zijlstra, J. J. P. (Hans) (1997). Geochemical engineering in chalk: Neutralization of waste sulfuric acid. *Ann. Soc. Géol. Du Nord, 5*, 345–350.

Dijk, P., & Berkowitz, B. (1998). Precipitation and dissolution of reactive solutes in fractures. *Water Resources Research, 34*(3), 457–470. https://doi.org/10.1029/97WR03238

Grosfils, P., & Lutsko, J. (2021). Impact of surface roughness on crystal nucleation. *Crystals, 11*(1), https://doi.org/10.3390/cryst11010004

Jayasekara, D., Ranjith, P., Wanniarachchi, W., Rathnaweera, T., & Chaudhuri, A. (2020). Effect of salinity on supercritical CO_2 permeability of caprock in deep saline aquifers: An experimental study. *Energy, 191*. https://doi.org/10.1016/j.energy.2019.116486

Jiang, Q., Hu, R., Deng, H., Ling, B., Yang, Z., & Chen, Y. (2025). Controls of the nucleation rate and advection rate on barite precipitation in fractured porous media. *Langmuir, 41*(2), 1250–1259. https://doi.org/10.1021/acs.langmuir.4c03532

Kampman, N., Bickle, M., Wigley, M., & Dubacq, B. (2014). Fluid flow and CO_2–fluid–mineral interactions during CO_2-storage in sedimentary basins. *Chemical Geology, 369*, 22–50. https://doi.org/10.1016/j.chemgeo.2013.11.012

Klasa, J., Ruiz-Agudo, E., Wang, L., Putnis, C., Valsami-Jones, E., Menneken, M., & Putnis, A. (2013). An atomic force microscopy study of the dissolution of calcite in the presence of phosphate ions. *Geochimica et Cosmochimica Acta, 117*, 115–128. https://doi.org/10.1016/j.gca.2013.03.025

Levenson, Y., Ryb, U., & Emmanuel, S. (2017). Comparison of field and laboratory weathering rates in carbonate rocks from an eastern mediterranean drainage basin. *Earth and Planetary Science Letters, 465*, 176–183. https://doi.org/10.1016/j.epsl.2017.02.031

Li, J., & Deepak, F. L. (2022). In Situ Kinetic Observations on Crystal Nucleation and Growth. *Chemical Reviews, 122*(23), 16911–16982. https://doi.org/10.1021/acs.chemrev.1c01067

Ling, B., Sodwatana, M., Kohli, A., Ross, C. M., Jew, A., Kovscek, A. R., & Battiato, I. (2022). Probing multiscale dissolution dynamics in natural rocks through microfluidics and compositional analysis. *Proceedings of the National Academy of Sciences, 119*(32), Article e2122520119. https://doi.org/10.1073/pnas.2122520119

Ma, X., Diao, Y., Fu, L., Yan, J., Yang, G., Zhang, C., et al. (2023). Comparison of water-caprock and CO_2-water-caprock geochemical reactivity in the triassic heshanggou formation of ordos basin. *International Journal of Greenhouse Gas Control, 124*. https://doi.org/10.1016/j.ijggc.2023.103860

Oelkers, E., & Schott, J. (2005). Geochemical aspects of CO_2 sequestration. *Chemical Geology, 217*(3–4), 183–186. https://doi.org/10.1016/j.chemgeo.2004.12.006

Poonoosamy, J., Haber-Pohlmeier, S., Deng, H., Deissmann, G., Klinkenberg, M., Gizatullin, B., et al. (2020). Combination of MRI and SEM to assess changes in the chemical properties and permeability of porous media due to barite precipitation. *Minerals, 10*(3), https://doi.org/10.3390/min10030226

Prieto, M., Astilleros, J., & Fernández-Díaz, L. (2013). Environmental remediation by crystallization of solid solutions. *Elements, 9*(3), 195–201. https://doi.org/10.2113/gselements.9.3.195

Rege, S., & Fogler, H. (1989). Competition among flow, dissolution, and precipitation in porous-media. *AIChE Journal, 35*(7), 1177–1185. https://doi.org/10.1002/aic.690350713

Ruiz-Agudo, E., Putnis, C., & Putnis, A. (2014). Coupled dissolution and precipitation at mineral-fluid interfaces. *Chemical Geology, 383*, 132–146. https://doi.org/10.1016/j.chemgeo.2014.06.007

Sabo, M. S., & Beckingham, L. E. (2021). Porosity-permeability evolution during simultaneous mineral dissolution and precipitation. *Water Resources Research, 57*(6), Article e2020WR029072. https://doi.org/10.1029/2020WR029072

Singurindy, O., & Berkowitz, B. (2003). Evolution of hydraulic conductivity by precipitation and dissolution in carbonate rock. *Water Resources Research, 39*(1), https://doi.org/10.1029/2001WR001055

Singurindy, O., & Berkowitz, B. (2005). The role of fractures on coupled dissolution and precipitation patterns in carbonate rocks. *Advances in Water Resources, 28*(5), 507–521. https://doi.org/10.1016/j.advwatres.2005.01.002

Stockmann, G., Wolff-Boenisch, D., Gislason, S., & Oelkers, E. (2011). Do carbonate precipitates affect dissolution kinetics? 1: Basaltic glass. *Chemical Geology, 284*(3–4), 306–316. https://doi.org/10.1016/j.chemgeo.2011.03.010

Stockmann, G., Wolff-Boenisch, D., Gislason, S., & Oelkers, E. (2013). Do carbonate precipitates affect dissolution kinetics? 2: Diopside. *Chemical Geology, 337*, 56–66. https://doi.org/10.1016/j.chemgeo.2012.11.014

Sudmalis, M., & Sheikholeslami, R. (2000). Coprecipitation of $CaCO_3$ and $CaSO_4$. *Canadian Journal of Chemical Engineering, 78*(1), 21–31. https://doi.org/10.1002/cjce.5450780106

Szymczak, P., & Ladd, A. (2009). Wormhole formation in dissolving fractures. *Journal of Geophysical Research-Solid Earth, 114*. https://doi.org/10.1029/2008JB006122

Tian, H., Xu, T., Li, Y., Yang, Z., & Wang, F. (2015). Evolution of sealing efficiency for CO_2 geological storage due to mineral alteration within a hydrogeologically heterogeneous caprock. *Applied Geochemistry, 63*, 380–397. https://doi.org/10.1016/j.apgeochem.2015.10.002

Wang, W., Li, X., Wei, Z., Xin, Y., Xiao, R., Yang, H., & Chen, X. (2023). Effect of CO_2-brine-rock interactions on the pore structure of the tight sandstone during CO_2 flooding: A case study of chang 7 member of the triassic yanchang formation in the ordos basin, China. *ACS Omega*. https://doi.org/10.1021/acsomega.2c06805

Xu, W., & Liu, C. (2025). Application of induced crystallization for the mitigation of calcium sulfate in high-sulfate wastewater: A review. *Journal of Water Process Engineering, 69*, Article 106824. https://doi.org/10.1016/j.jwpe.2024.106824

Yang, G., Ma, X., Feng, T., Yu, Y., Yin, S., Huang, M., & Wang, Y. (2020). Geochemical modelling of the evolution of caprock sealing capacity at the shenhua CCS demonstration project. *Minerals, 10*(11), https://doi.org/10.3390/min10111009

Zhou, C., Hu, R., Li, H., Yang, Z., & Chen, Y. (2022). Pore-scale visualization and quantification of dissolution in microfluidic rough channels. *Water Resources Research, 58*(11), https://doi.org/10.1029/2022WR032255

Zhou, C. X., Hu, R., Deng, H., Ling, B., Yang, Z., & Chen, Y. F. (2023). Surface-volume scaling controlled by dissolution regimes in a multiphase flow environment. *Geophysical Research Letters, 50*(18), Article e2023GL104067. https://doi.org/10.1029/2023GL104067